ECS Journal of Solid State
Science and Technology

OPEN ACCESS

Synthesis and Characterization of Cr-Doped $Pb_2Fe_2O_5$ Thin Films by Reactive Magnetron Sputtering

To cite this article: Benas Beklešovas *et al* 2023 *ECS J. Solid State Sci. Technol.* **12** 103014

ECS Journal of Solid State Science and Technology, 2023 **12** 103014

Synthesis and Characterization of Cr-Doped $Pb_2Fe_2O_5$ Thin Films by Reactive Magnetron Sputtering

Benas Beklešovas,[1,z] Vytautas Stankus,[1] Brigita Abakevičienė,[1] Joosep Link,[2] Raivo Stern,[2] Artyom Plyushch,[3] Jūras Banys,[3] Jurgita Čyvienė,[1] Rolandas Girčys,[4] Matas Bašinskas,[1] and Evaldas Kalvaitis[5]

[1]*Department of Physics, Kaunas University of Technology, LT-51368 Kaunas, Lithuania*
[2]*Laboratory of Chemical Physics, National Institute of Chemical Physics and Biophysics, EE-12618 Tallinn, Estonia*
[3]*Faculty of Physics, Vilnius University, Vilnius, LT-10222, Lithuania*
[4]*Department of Computer Sciences, Kaunas University of Technology, LT-51368 Kaunas, Lithuania*
[5]*Health Telematics Science Institute, Kaunas University of Technology, LT-51423 Kaunas, Lithuania*

Multiferroic materials, which exhibit simultaneous ferroelectricity, ferromagnetism, and ferro-elasticity, have attracted significant attention due to their multifunctional properties. Coupling between ferroelectric and magnetic properties has led to the development of non-volatile memory devices, transducers, magnetic field sensors, and other applications. $Pb_2Fe_2O_5$ (PFO) is a promising multiferroic material due to it simultaneously exhibiting ferroelectricity and ferromagnetism at room temperature. Doping with aliovalent ions, such as Cr^{3+}, has been proposed as an effective method for enhancing the ferroelectric and magnetic properties, consequently leading to the enhancement of multiferroic properties. The investigation shows that the lead ferrite phase (220) was present in all samples, but its abundance reduced with increasing synthesis temperature due to lead desorption. Dielectric measurements revealed that PFO films with highest Cr concentration had the highest polarization (P_r) of 72.2 μC cm^{-2}. The study also found that the magnetization of PFO films was up to $9.5{\cdot}10^{-7}$ μAm^2 at an ambient temperature of 5 K, and the magnetic ordering temperature was 363 K, corresponding to the magnetic ordering temperature of chromium oxides. The morphology of Cr doped PFO films changed with increasing chromium content, resulting in a reduction in grain size and an increase in the film density.

 [DOI: 10.1149/2162-8777/ad0324]

Manuscript submitted July 11, 2023; revised manuscript received September 11, 2023. Published October 27, 2023.

Multiferroic materials simultaneously exhibit different primary ferroic properties, including ferroelectricity, ferromagnetism, and ferroelasticity, rendering them multifunctional materials.[1–4] Of particular interest is the coupling between ferroelectric and magnetic properties, which has received considerable attention. The ability to manipulate both ferroelectric and magnetic properties in a single phase presents numerous opportunities for the development of non-volatile memory devices,[5] transducers,[6] magnetic field sensors,[6] and other applications.[7,8] Solid state memory devices have been subjected to special attention due to the ability of multiferroics to enable electric writing and magnetic reading, leading to high storage density and low power consumption.[6] The two mechanisms involved in this process are ferroelectricity, which arises from transition ions with empty d shells, and magnetism, which requires transition metal ions with partially filled d shells.[1,2,9] Many multiferroic materials encounter limitations, such as a low Néel temperature, which restricts their suitability for room temperature applications.[10,11] Consequently, there exists a demand to explore novel multiferroics or enhance the existing ones. Notably, substantial progress has been achieved over the last 15 years in the exploration and advancement of multiferroic materials.[7] One such promising multiferroic, an $ABO_{3-\delta}$ perovskite type oxide ($0 \leqslant \delta \leqslant 0.5$, A = Lanthanide or alkaline Earth, B = transition metal) is lead ferrite $Pb_2Fe_2O_5$ (PFO), which has been reported to exhibit both ferroelectric and magnetic properties at room temperature . The non-centrosymmetric structure, resulting from the effect of the $6s^2$ lone pair and covalent Pb–O bonds, is responsible for the ferroelectricity, while the magnetization arises from the B site (Fe^{3+}).[12] The coexistence of ferroelectricity and ferromagnetism has been observed in PFO ceramics, with a remnant polarization estimated to be ~0.22 μC cm^{-2} at room temperature.[12] The previous study demonstrated the successful deposition of PFO thin films with a remnant polarization of 60,9 μC cm^{-2}, which indicates promising applications for PFO.[13]

Particular attention should be dedicated to addressing the challenges related to high leakage current and lower magnetoelectric coupling coefficients. Doping is considered a highly effective method for modifying the fundamental properties of multiferroics to address these issues.[14–16] The properties of PFO can be altered through the substitution of Pb^{2+} (A-site) and Fe^{3+} (B-site) ions. The Fe^{3+} ion at the B-site, with a radius of 0.64 Å, is similar in size to other ions such as Cr^{3+} (0.76 Å), Ti^{4+} (0.68 Å), and Mn^{3+} (0.72 Å), making them potential substitutes for Fe^{3+}.[7,17,18] However, using aliovalent dopants necessitates charge compensation to maintain charge neutrality and avoid oxygen vacancies, which can be achieved by using isovalent ions such as Cr^{3+}.[19] The B-site of PFO can be occupied randomly by Fe^{3+} and Cr^{3+} ions, which may cause distortion of the cation spacing between oxygen octahedra.[14,20,21] Previous studies have reported that the structure of PFO is periodically modulated by crystallographic shear planes.[22] The displacement vector of these planes can be represented by $\vec{R} = 1/2[110]_p + 1/3[001]_p$, where the $1/2[110]_p$ term is the shear operation vector and $1/3[001]_p$ is the relaxation part.[23] This structural arrangement leads to different superexchange interactions between corner-sharing Fe–O polyhedral and adjacent blocks across the common edges of the Fe–O_5 tetrahedral pyramids.[24] The incorporation of Cr^{3+} into the structure may result in spin coupling between Fe^{3+}–O–Cr^{3+} that could potentially enhance the magnetic and ferroelectric properties of PFO.[21,25,26] Up to this point, there have been no reports on doping PFO with transition group metals. Therefore, the impact of chromium doping on the ferroelectric and magnetic properties of PFO thin films will be examined.

Experimental

The layer-by-layer reactive magnetron sputtering method was employed[27] to deposit chromium-doped lead ferrite thin films. For this purpose, a platinized silicon Pt/Ti/SiO_2/Si multilayer system was used as a substrate. The utilization of a platinized silicon substrate was necessitated by the inherent challenges associated with oxide thin films adhering to SiO_2/Si substrates. Furthermore, platinum

[z]E-mail: benas.beklesovas@ktu.edu

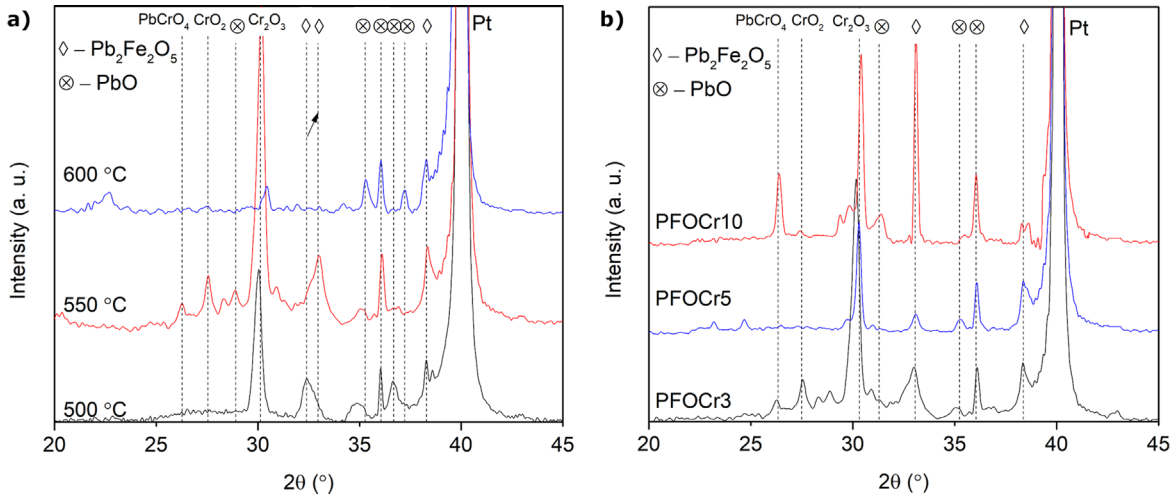

Figure 1. (a) XRD spectra of PFOCr5 formed at different synthesis temperatures; (b) XRD spectra of Cr doped PFO formed at 550 °C at different Cr concentrations.

serves as a highly beneficial foundational electrode material in this context. Each magnetron was equipped with a single element (Pb, Fe, and Cr) high-purity target (Kurt J. Lesker Company). The target was 3 inches in diameter, disc shape, with purity levels reaching 99.9%. The starting pressure was $5{\cdot}10^{-3}$ Pa. The distance between the target and substrate was kept at 60 mm. The quality of the films heavily depends on the seeding layer, and thus, titanium was chosen for this reason.[28] A Ti seeding layer was synthesized by reactive magnetron sputtering in a pure argon gas environment, with a working pressure of 1.3 Pa, a substrate temperature of 750 °C, and a duration time selected to achieve a thickness of 5 nm. Ti seeding layer enhances adhesion, effectively prevents issues like delamination and peeling. Immediately after the deposition of the seeding layer, the gas environment was changed to O_2 while maintaining the same working pressure of 1.3 Pa, and the substrate temperature was reduced to one of the specified synthesis temperatures of 500 °C, 550 °C and 600 °C. Lead ferrite thin films were formed in situ by moving the substrate above the three continuously active magnetrons for a duration of 1 h which allowed to reach film thickness up to 900 nm. The substrate holder underwent periodic perpendicular motion relative to the magnetrons, oscillating at a frequency of 0.5 Hz. This regulated motion served to ensure that the deposited layers achieved a suitable thickness, thereby facilitating effective chemical interactions among all deposited elements. The power of Fe, Pb, and Cr magnetrons was kept at 110 W, 550 W, and 70 W, respectively. The sputtering rate of Cr was controlled by adjusting the slit over the Cr magnetron. Finally, aluminum top electrodes with an oval shape and a diameter of 1.3 mm were formed by using thermal evaporation method. To explore the influence of Cr on the structure, dielectric properties, and magnetic characteristics of PFO films, doping with various concentrations of Cr (0.03 wt%, 0.05 wt%, and 0.1 wt%) was performed. These films are referred to as PFOCr3, PFOCr5, and PFOCr10, respectively, indicating the respective Cr concentrations.

The PFO film's X-ray diffraction (XRD) patterns were obtained using monochromatic CuKα radiation with Bruker D8 series (Bruker, Billerica, Massachusetts, USA) diffractometer, utilizing Bragg-Brentano geometry. Ferroelectric hysteresis loop measurements of the films were conducted using the Sawyer - Tower method. The circuit consisted of a 1 kΩ resistor and a reference capacitor of 150 nF, operating at a frequency of 50 Hz and a temperature of 25 °C. The "TF Analyzer 2000E" (aixACCT Systems GmbH, Aachen, Germany) measuring equipment was used for dielectric measurements. Scanning electron microscopy (SEM) imaging was carried out with the S-3400N measurement system (Hitachi High-Technologies corp., Tokyo, Japan) using a 10 kV operating voltage. Magnetic properties were measured with the Vibrating Sample Magnetometer option of the Quantum Design Physical Property Measurement System (QD PPMS, Quantum Design, San Diego, California, USA). Atomic force microscopy (AFM) measurements were conducted using the JPK NanoWizard 3 system (Bruker, Billerica, Massachusetts, USA). For the quantification of surface roughness, a silicon ACTA probe (Applied NanoStructures Inc., Santa Clara, California, USA) with specific parameters, including a tip radius of less than 6 nm, a height of 14-16 mm, and a spring constant of 40 N m^{-1}, was utilized. These measurements were conducted in tapping mode as the probe traversed the sample surfaces.

Results and Discussion

Structure properties.—As shown in Fig. 1a, the lead ferrite phases' (220) and (312) peaks are observable at 32° and 38° angles (PDF# 33-0756 card), respectively, when the synthesis temperature is 500 °C. As the synthesis temperature is raised while maintaining the same concentration of Cr, the PFO (220) phase peak is observed to shift towards higher angles. Cr tends to occupy lattice positions, thereby modifying atomic spacing within the crystal lattice. This alteration subsequently induces an increase in the X-ray diffraction angle, leading to a shift of peaks towards higher angles. In this specific case, the 2θ angle demonstrates an increase from 32.4° to 32.9°, which could potentially signify a more active exchange of Fe^{3+} ions for Cr^{3+} ions. When the synthesis temperature is further increased to 550 °C, the secondary phases of $PbCrO_4$ and CrO_2 are detected at angles of 26.3° and 27.5°, respectively, along with a more intense peak of Cr_2O_3 at 30°. Subsequently, a substantial reduction in the intensity of the PFO (220) phase peak was observed at a substrate temperature of 600 °C due to lead evaporation or desorption, while the (312) phase peak exhibited relatively stable characteristics. In addition, a texturing effect is observed.

The XRD spectrum in Fig. 1b shows a clear modification in the PFO structure resulting from the variation in Cr concentration under the same synthesis temperature (550 °C). At angles of 32.9° and 38°, peaks of (220) and (312) PFO phases are identified. With an increase in the Cr concentration of PFO (220), the peak slightly shifts from 32.9° to 33.1°, likely due to the substitution of larger chromium ions for smaller iron ions, resulting in lattice distortion. Additionally, an upsurge in the peak intensity of the PFO phase is observed. However, an increase in Cr concentration leads to the formation of secondary phases. A phase peak of $PbCrO_4$ at 26°, CrO_2 at 27.5°,

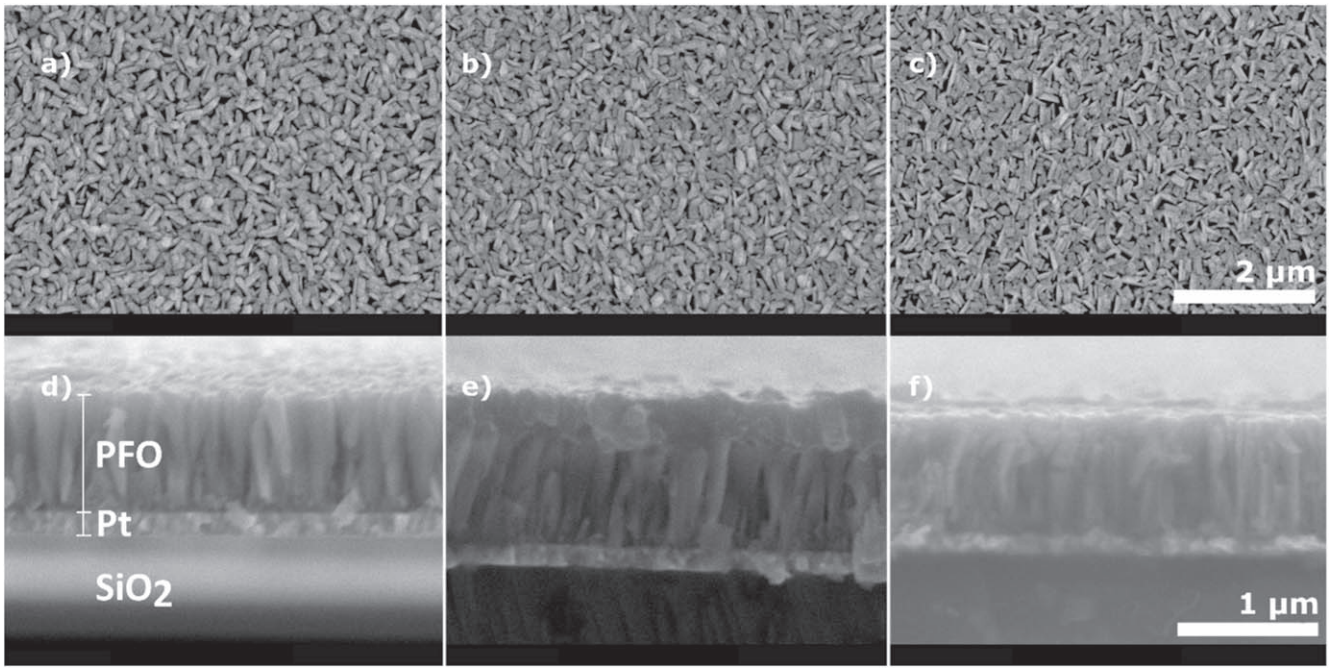

Figure 2. SEM surface images of Cr doped PFO synthesized at 550 °C: (a) PFOCr3; (b) PFOCr5; (c) PFOCr10 and cross section images: (d) PFOCr3; (e) PFOCr5; (c) PFOCr10.

and Cr_2O_3 at approximately 30° are detected. Lead oxide is detected at angles of 29°, 31°, 35°, 36° and 37°. In their studies, A. M. Abakumov[22] and M. Wang[12] found that due to the formation of crystallographic planes and defects during synthesis, the chemical formula of lead ferrite is defined as $Pb_{0.9375}FeO_{2.4375}$, $Pb_{0.9}FeO_{2.4}$, and $Pb_{0.875}FeO_{2.375}$, which are described by the general formula $PbFeO_{2.5-x}PbO$ (where x = 0.0625, 0.1, and 0.125).[12,22] As can be seen from the general formula, it is difficult to avoid the formation of secondary lead oxide phases, as seen in the XRD spectrum in Fig. 1.

The observed reduction in grain size is evident when comparing samples PFOCr3 to PFOCr10, synthesized at 550 °C, with an increase in Cr concentration. Specifically, the grain size decreases from approximately 270 nm (Fig. 2a) to 230 nm (Fig. 2c). During synthesis, dopant elements have low mobility, which restricts their diffusion and formation of new nucleation centers upon reaching the film surface. A higher density of nucleation centers results in smaller (or denser) grains. In the studies of by J. N. B. Sales[29] and other researchers,[30] the influence of impurities on another ABO_3 perovskite material ($BiFeO_3$) was analyzed, and it was found that the Zenner model mechanism determines the grain size, where secondary phase particles hinder grain growth by capturing the grain boundary, thereby stopping its expansion upon collision with another particle. Additionally, the size of structures can be affected by chromium's reduced concentration of oxygen vacancies, which limits ion diffusion.[15] Cross-sectional images reveal dense columnar formation in all films, with thickness ranging from approximately 850 nm.

Figure 3 compares PFOCr5 films that were formed in the temperature range of 500 °C–600 °C. Densely arranged structures with clearly defined boundaries are visible. As the synthesis temperature increases from 500 °C (Fig. 3a) to 600 °C (Fig. 3c), an increase in the diameter of the structures (grains) can be observed. The grains reach an average size of 250 nm, 325 nm and 510 nm at the respective synthesis temperatures of 500 °C, 550 °C and 600 °C. The growth of the grain size is directly influenced by the synthesis temperature, which, being higher, gives the adatoms more energy so that they can continue to diffuse to the nucleation centers and form larger structures.[31] Upon analysis of cross-sectional images (Figs. 3d to 3f), it is to be observed that the structures under investigation exhibit predominantly dense arrangements. However, it is pertinent to acknowledge that as the grain size increases, certain voids become discernible, notwithstanding the absence of substantial structural defects or extraneous inclusions. Columnar growth predominates in all samples. This columnar growth appears to be continuous, as evidenced by the consistent and unbroken pattern of columns extending from the substrate surface throughout the film. Moreover, the surface exhibits a relatively uniform and smooth appearance, which can be attributed to the alignment of these columns. The most densely arranged columns are observed in the sample formed at 600 °C, which could have an impact on the ferroelectric properties.

The chemical composition analysis of the PFOCr5 thin film synthesized at 550 °C was conducted using the Energy-Dispersive X-ray Spectroscopy (EDS) technique, with the corresponding results presented in Fig. 4. The obtained data confirms the presence of essential elements, namely lead (Pb), iron (Fe), oxygen (O), as well as the substituted element Cr. A detailed element mapping, as indicated in the inset, illustrates the uniform distribution of Pb (purple), Fe (blue), and Cr (red) elements within the synthesized sample. This observation strongly supports the uniform substitution of Cr within the PFO thin film, consistent with the findings from XRD analysis. Additionally, traces of other elements such as platinum (Pt), silicon (Si), aluminum (Al), and carbon (C) are also detected. The occurrence of Pt, Si, and Al can be attributed to the electrode materials, which include platinized silicon for the bottom electrode and aluminum for the top electrode. The minimal presence of C is attributed to environmental contamination during the sample handling process.

In Fig. 5, atomic force microscope topography images (10 μm × 10 μm) of PFOCr5 films are presented. The film formed at 500 °C exhibited an average roughness of 17.73 nm and a geometrical roughness of 22.33 nm, with a difference between the highest peak and the lowest measured point (R_t) of 191.8 nm, as shown in Figs. 5a and 5d. Increasing the synthesis temperature to 550 °C, as shown in Figs. 5b and 5e, resulted in the formation of larger structures, leading to a higher surface roughness, with the R_a value reaching 27.67 nm and R_q reaching 35.26 nm. The R_t value increased by approximately 30% and reached 315.1 nm. The increase in the dimensions of the structures with the synthesis temperature can be related to the energy gained by the atoms and surface diffusion (Table I). At higher

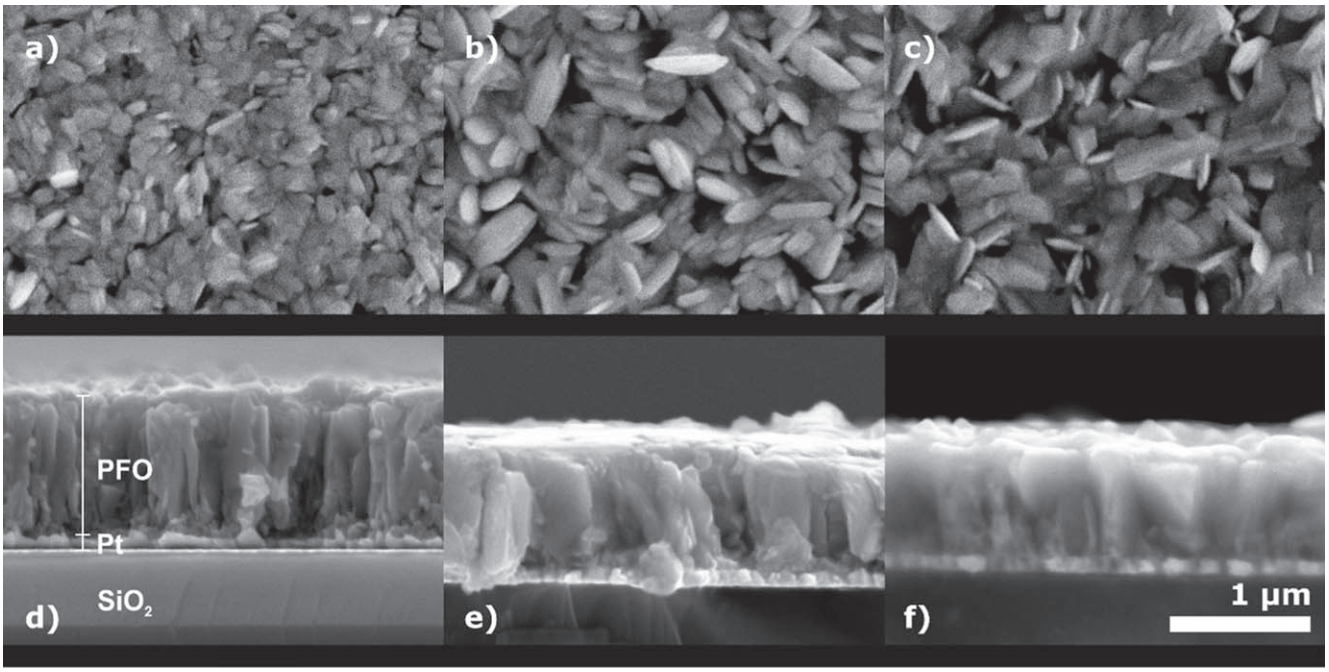

Figure 3. SEM images of PFOCr5 films deposited at: (a) 500 °C; (b) 550 °C; (c) 600 °C and cross-sectional images: (d) 500 °C; (e) 550 °C; (c) 600 °C.

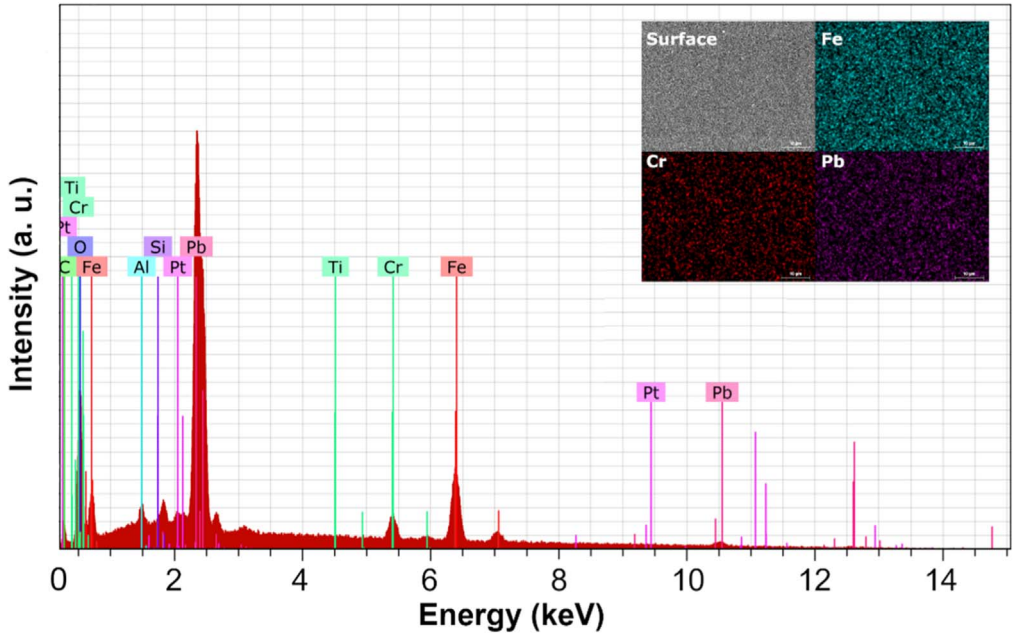

Figure 4. EDS spectroscopy pattern of PFOCr5. Inset figures are the element mapping of Pb, Fe and Cr.

synthesis temperatures, the atoms that reach the surface possess higher energy, enabling them to diffuse more extensively along the surface towards the nucleation centers, which, consequently, allows formation of larger structures. In contrast, atoms with lower energy exhibit limited diffusion, causing the nucleation centers to be more densely packed and resulting in smaller structures. Deepak et al.[32] and other researchers[33,34] also found an increase in grain size with synthesis temperature while analyzing the morphology dependence of another multiferroic, BFO.

Ferroelectric properties.—Figures 6a–6c shows the dependence of polarization hysteresis loops of chromium-doped PFO films on external electric field (at 12.5 V and 50 Hz) for different chromium concentrations and synthesis temperatures in the range of 500 °C–600 °C. Figure 6a presents the P-E dependence as a function of chromium concentration when synthesis temperature was 500 °C. The obtained hysteresis loops have an oval shape, indicating the existence of leakage currents in all samples.[35] PFOCr3 and PFOCr5 samples reach the same 97 μC cm^{-2} saturation, which starts to decrease uniformly from an external electric field value of 171 kV cm^{-1}, while the PFOCr10 sample saturates to 108 μC cm^{-2}. The remnant polarization values of PFOCr3, PFOCr5, and PFOCr10 films are 65.4 μC cm^{-2}, 72.2 μC cm^{-2}, and 69.9 μC cm^{-2}, respectively, with corresponding coercive field (E_c) values of 97.1 kV cm^{-1}, 102.9 kV cm^{-1}, and 105.7 kV cm^{-1}.

Increase of the synthesis temperature to 550 °C for PFOCr3 and PFOCr5 samples (Fig. 6b) yields a more evident alteration in remnant polarization under an external electric field. This

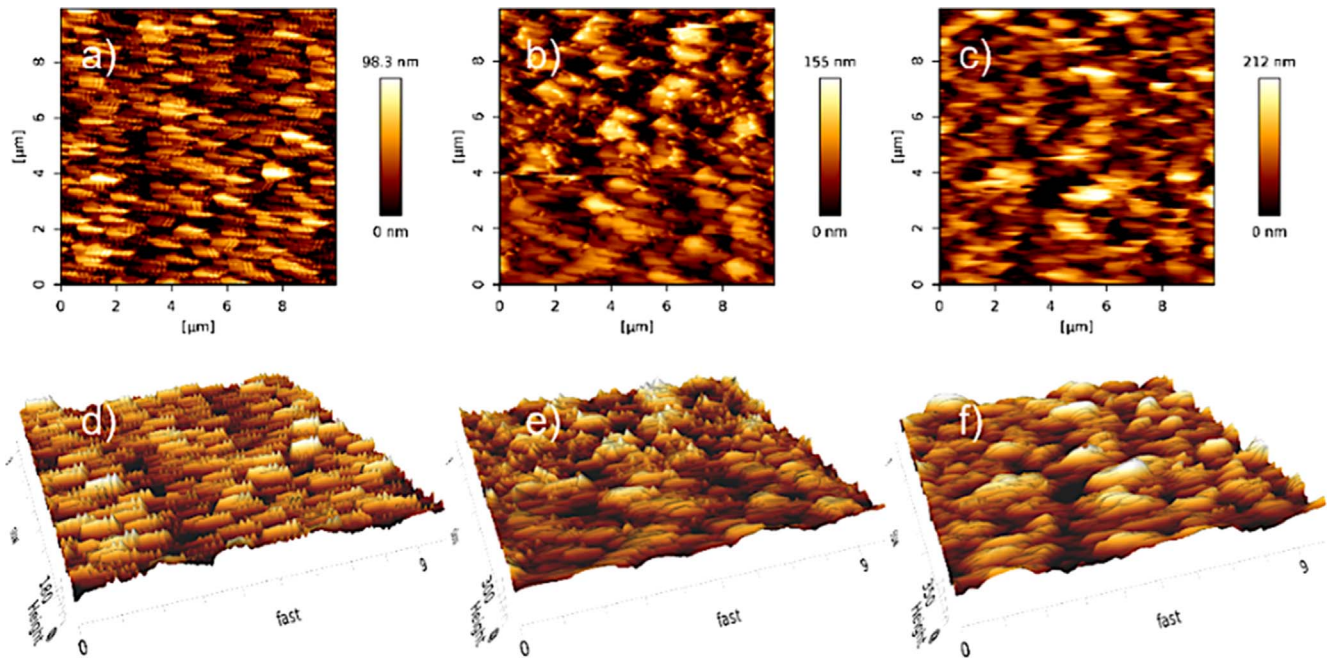

Figure 5. AFM surface images of PFOCr5 deposited at: (a) 500 °C; (b) 550 °C; (c) 600 °C; and three-dimensional images: (d) 500 °C; (e) 550 °C; (f) 600 °C.

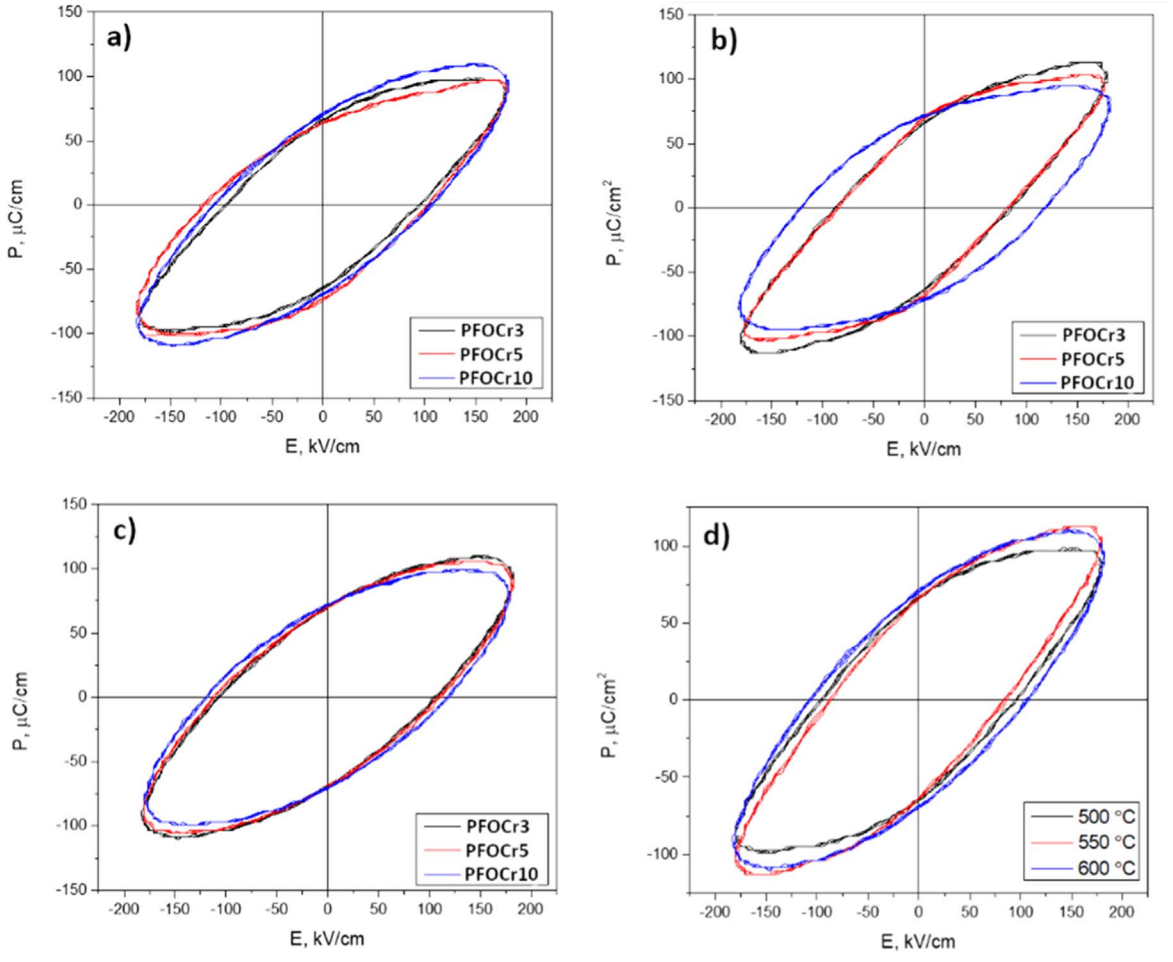

Figure 6. Dependence of the polarization of PFO doped with chromium on the electric field at the synthesis temperature: (a) 500 °C; (b) 550 °C; (c) 600 °C; and (d) PFOCr5 synthesized at different temperature polarization dependence on the electric field.

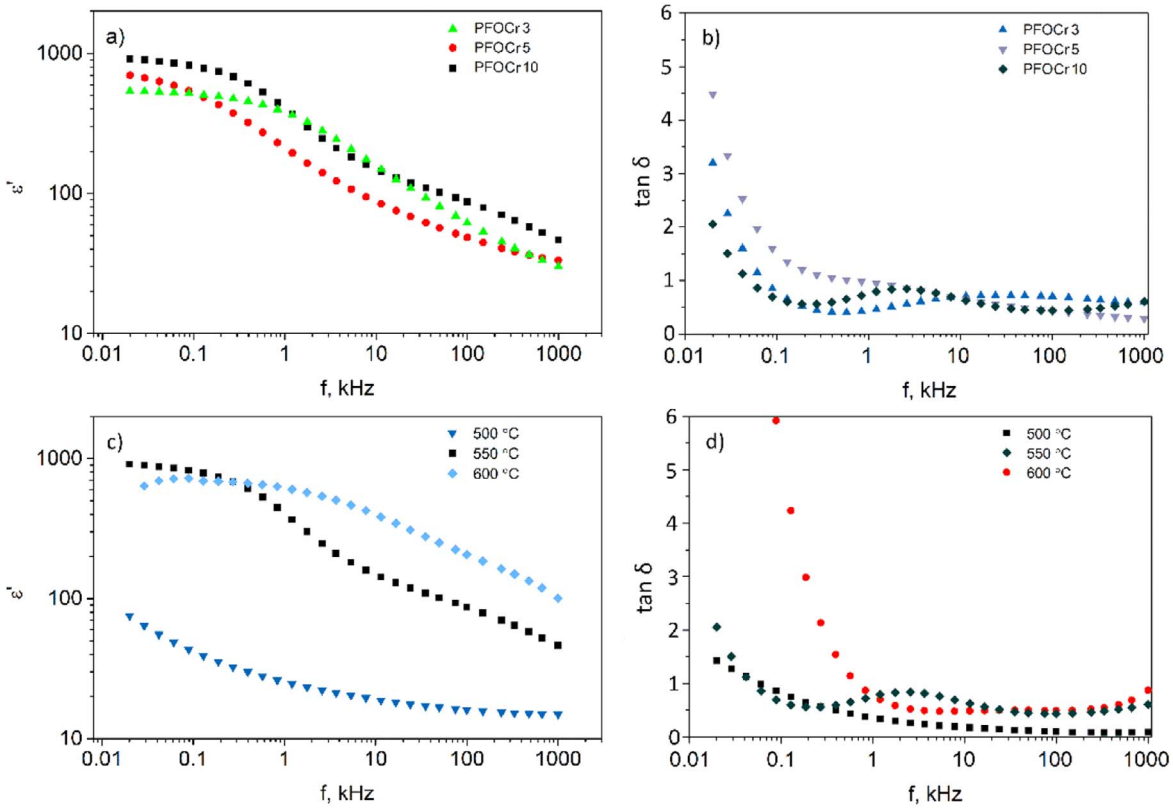

Figure 7. Dependence of dielectric permittivity (a) and loss tangent (b) on the external electrical field frequency for Cr-doped PFO thin films synthesized at 550 °C with different Cr concentrations; Dependence of dielectric permittivity (c) and loss tangent (d) on the external electrical field frequency for PFOCr10 films synthesized at different temperatures.

Table I. The impact of synthesis temperature on the surface topography of PFOCr5.

Synthesis temperature, °C	Average roughness (R_a), nm	RMS roughness (R_q), nm	Distance between lowest and highest points (R_t), nm
500	17.73	22.33	191.8
550	27.61	35.26	315.1
600	37.51	48.21	386.1

observation suggests the possibility of reduced leakage currents in the samples. The obtained P_r values slightly changed for PFOCr3, PFOCr5, and PFOCr10 samples—65.4 μC cm^{-2}, 69.9 μC cm^{-2}, and 69.9 μC cm^{-2}, respectively, with corresponding E_c values of 86.9 kV cm^{-1}, 87 kV cm^{-1}, and 118.9 kV cm^{-1}. At synthesis temperature of 600 °C (Fig. 6c), the oval shape of hysteresis loops remains due to leakage currents in the films. The obtained P_r values slightly decreased compared to those of films formed at 500 °C and 550 °C. The remnant polarization values of PFOCr3, PFOCr5, and PFOCr10 films are 65.4 μC cm^{-2}, 65.4 μC cm^{-2}, and 69.9 μC cm^{-2}, respectively, with corresponding E_c values of 97.1 kV cm^{-1}, 86.9 kV cm^{-1}, and 106.8 kV cm^{-1}.

In all cases, an improvement of ferroelectric properties was observed by increasing the chromium concentration to the corresponding level. This can be explained by compensation of the positive charge defect due to Pb vacancy, which can also affect the formation of oxygen vacancies in the films. The perovskite ABO_3 phase distortion is caused by oxygen vacancies, which restrict the movement of B site ions and affect the remnant polarization.[16] It is believed that the higher coercive field values in the doped PFO samples are due to the displacement of Cr^{3+} ions from the centrosymmetric location in the octahedron, thus impeding the polarization reversal.[36]

Figure 6d illustrates the relationship between the hysteresis loops of PFOCr5 and the synthesis temperature. The hysteresis loops maintain a very similar shape with a gradual polarization change at the saturation polarization, where the values of P_r reach 97 μC cm^{-2}, 108 μC cm^{-2}, 112 μC cm^{-2} at the corresponding synthesis temperatures of 500 °C, 550 °C, and 600 °C. It can be concluded that temperature does not have a significant effect on eliminating leakage currents. The variation in Cr concentration potentially influences the size of crystallites, as observed in the XRD spectra (Fig. 1). An increase in concentration corresponds to a reduction in crystallite size, subsequently altering the ratio of grain boundaries to the volume of the crystallites. The increase in chromium content, which replaces Fe ions, causes distortion of the lattice which may lead to higher polarization values.

Dielectric properties.—Figure 7 presents the frequency characteristics of the dielectric permittivity of Cr doped PFO films at room temperature. The analysis was conducted on samples synthesized at different temperatures and with varying chromium concentrations. Figure 7a illustrates the relationship between the real part of the dielectric permittivity and the frequency for the PFOCr3, PFOCr5, and PFOCr10 samples, which were synthesized at 550 °C. As observed, ε' consistently decreases in all samples.

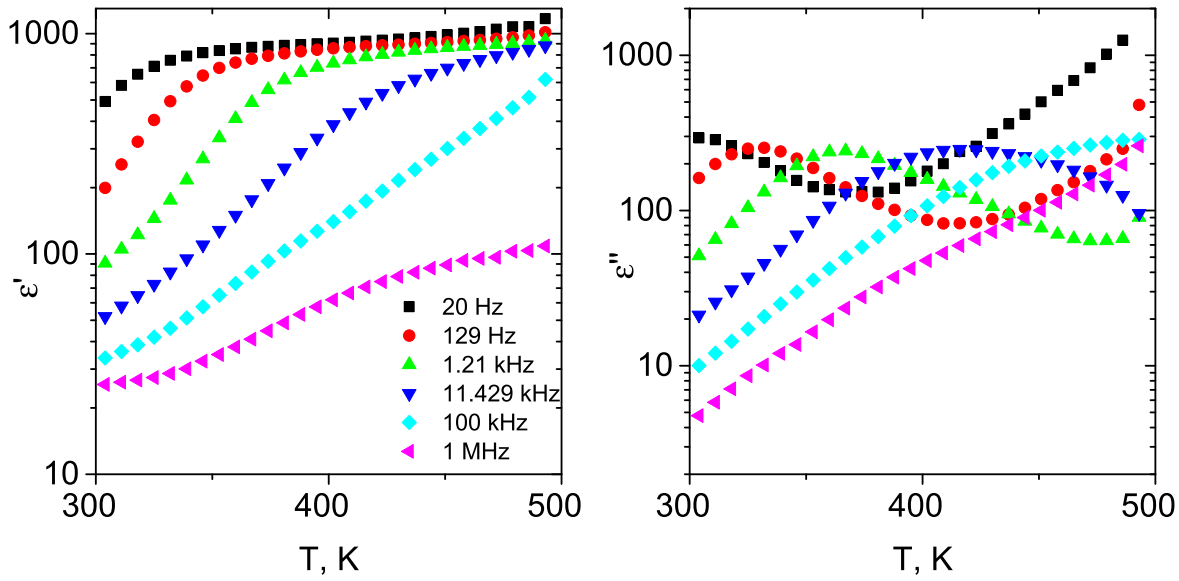

Figure 8. Complex dielectric permittivity dependence on the temperature of PFOCr10 samples synthesized at 550 °C.

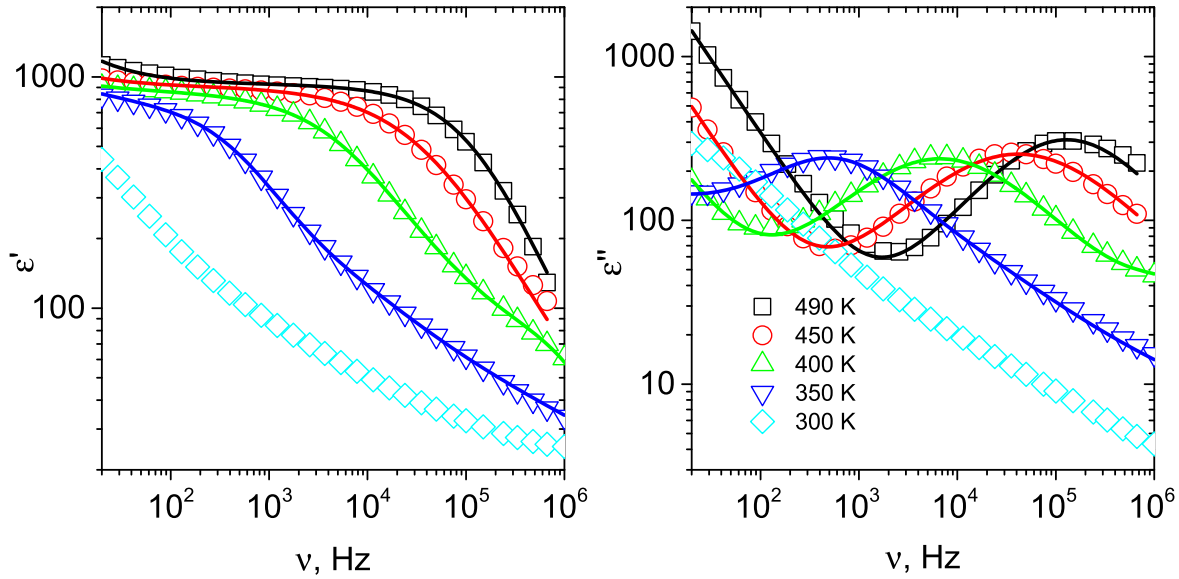

Figure 9. Dielectric permittivity dependence on the frequency of PFOCr10 synthesized at 550 °C. Symbols stand for the experimental data, and solid lines denote the approximation with Eq. 1.

The dynamics of the ε′ values were similar for the group of films deposited at the same temperature (550 °C) but with different chromium concentrations, ranging from 530–900 to 30–46 in the frequency range of 20 Hz to 1 MHz. The dipoles no longer had time to change their orientation in the rapidly oscillating electric field, resulting in a gradual decrease in dielectric permittivity across all films as the frequency of the electric field increased. When analyzing the dependence of the loss tangent on frequency in Fig. 7b, it can be observed that the maximum values of the loss tangent prevail in the low-frequency range (20–200 Hz interval). All films exhibit relatively high values of the loss tangent, possibly due to the presence of leakage currents in the films (active current).[1] As the frequency of the electric field increases further, up to 1 kHz, the values of the loss tangent stabilize and show little change in the remaining frequency range up to 1 MHz. Figure 7c presents the dependence of the dielectric permittivity of PFOCr10 films deposited at different synthesis temperatures on the external electric field frequency. In this case, the film formed at 500 °C exhibited the lowest ε′ value among the entire group of samples, and as the frequency increased from 20 Hz to 1 MHz, it decreased from 75 to 15, respectively. When examining the dependence of the loss tangent on the external electric field frequency for the same set of samples (Fig. 7d), the film with the highest chromium concentration (PFOCr10) and synthesis temperature (600 °C) showed the highest loss tangent.

In order to study the dynamics of the dipoles polarization measurements at different temperatures were carried out. The typical dependence of the complex dielectric permittivity is presented in Fig. 8. Noticeable frequency dispersion in real part is accompanied with maximum of the imaginary part of the permittivity. As frequency increases the maximum shifts to a higher temperature. The frequency spectra of permittivity demonstrate similar relaxation behavior (Fig. 9, symbols). The dependencies of all samples were approximated with Cole-Cole function (Fig. 9, solid curves):

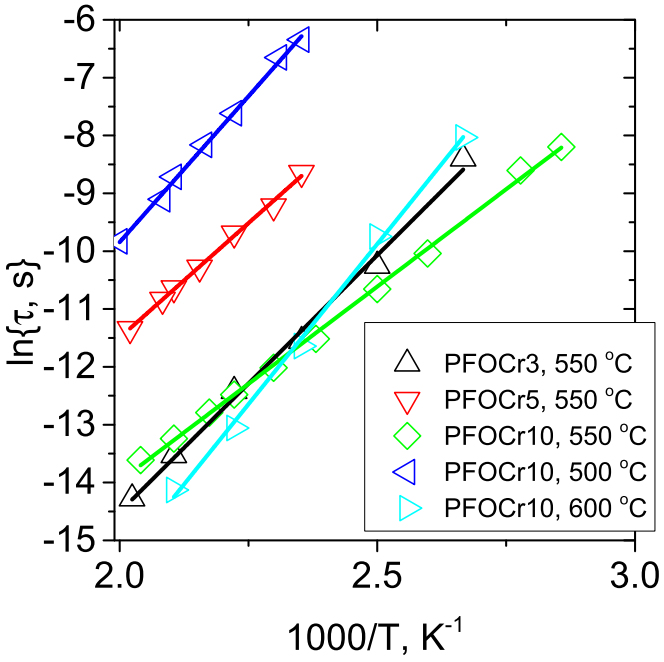

Figure 10. Relaxation time as a function of temperature. Symbols stand for the experimental data, and solid lines denote the approximation with Eq. 1.

$$\varepsilon = \sum_{i=1}^{2} \frac{\Delta\varepsilon_i}{1 - (j\omega\tau_i)^{1-\alpha}}, \qquad [1]$$

where $\Delta\varepsilon = \varepsilon_s - \varepsilon_\infty$ is a difference between static and high-frequency limits of permittivity, $\omega = 2\pi\nu$ is an angular frequency, τ is a relaxation time and $\alpha \in (0, 1)$ denotes the broadness of the relaxation process. Each term in Eq. 1 represents one relaxation process, i.e. a maximum in the imaginary part of permittivity and corresponding decrease in ε'. One of the relaxation occurs below the studied range of frequency. All parameters in Eq. 1 depend on temperature. The relaxation time of the high-frequency process decreases following the Arrhenius law:

$$\tau = \tau_0 e^{\frac{Ea}{kT}}, \qquad [2]$$

Where E_a is an activation energy, and $k = 8.617 \cdot 10^{-5}$ eV K^{-1} is a Boltzmann constant. Both experimental results and fits are collected in Fig. 10 and in Table II. The synthesis temperature could have a greater impact on the film structure, as well as on the concentration of defects and the composition of the structure. In summary, the dynamics of the dielectric permittivity of all samples with respect to the electric field frequency can be explained as a result of migration polarization in the low-frequency region. As the chromium concentration increases, the grain size decreases, thereby increasing the ratio between grains and intergranular boundaries. The increase in chromium content and synthesis temperature may affect the growth of defect concentration. These defects can act as barriers to charge carriers, thereby creating local polarization. It is worth mentioning that the conductivity of the films can also be influenced by oxygen vacancies, the concentration of which increases at higher synthesis temperatures.[7,37]

Magnetic properties.—In Fig. 11a, it was found from isothermal magnetization measurements that films synthesized at 550 °C with different chromium concentrations exhibited a dependence on hysteresis loop shape. The remanent magnetization between PFOCr5 and PFOCr10 varied slightly, reaching values of $2.08 \cdot 10^{-8}$ Am^2 to $2.86 \cdot 10^{-8}$ Am^2. The coercive field also varied little between samples, ranging from 3.1 to 8 mT. Figure 11b shows the visible influence of chromium on the magnetic properties of PFO at 5 K ambient temperature. In this case, better magnetic properties were obtained, as the saturation values of the magnetic moment increased with the Cr concentration and reached $7.5 \cdot 10^{-7}$ Am^2, $8.8 \cdot 10^{-7}$ Am^2, and $9.5 \cdot 10^{-7}$ Am^2, respectively. The recorded remanent magnetization also increased with chromium concentration, reaching $2.2 \cdot 10^{-8}$ Am^2, $2.6 \cdot 10^{-8}$ Am^2, and $3.2 \cdot 10^{-7}$ Am^2, respectively. One possible reason for the enhancement of magnetic properties with an increase in Cr concentration could be the insertion of a Cr^{3+} ion instead of Fe^{3+}, which changes the Fe–O–Fe bond angle due to a distorted lattice.[14,38]

In Fig. 12, the temperature dependencies of magnetization of chromium-doped films during Field Cooling (FC) and Zero Field

Table II. Activation energy for different samples.

Sample	PFOCr3, 550 °C	PFOCr5, 550 °C	PFOCr10, 550 °C	PFOCr10, 500 °C	PFOCr10, 500 °C
E_a, eV	0.765	0.68316	0.5799	0.86971	0.95531

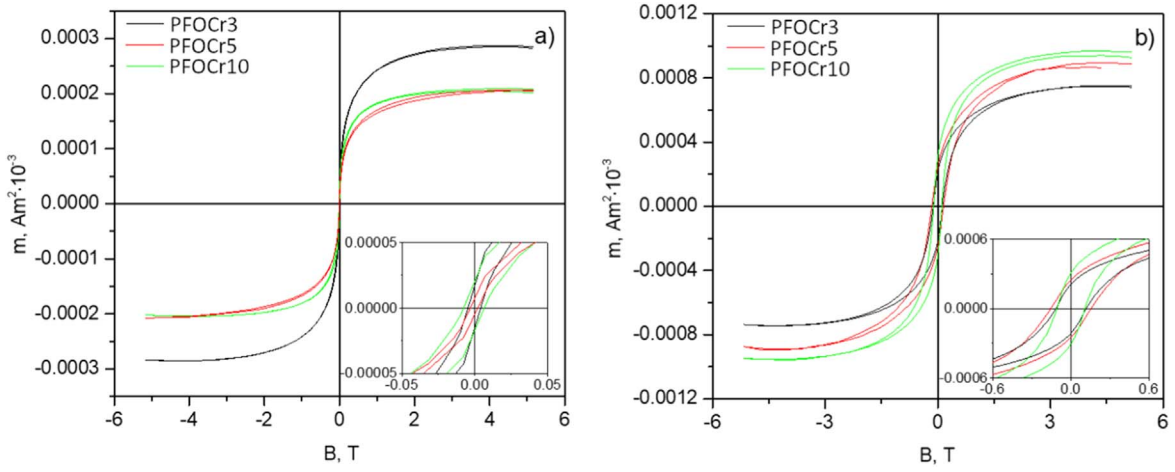

Figure 11. Dependence of PFO magnetic moment on Cr concentration at ambient temperatures: (a) 300 K; (b) 5 K.

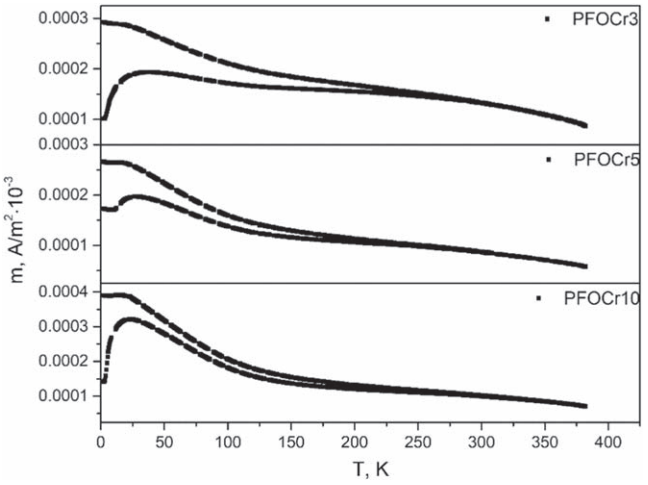

Figure 12. ZFC-FC curves of PFO doped with various Cr concentrations.

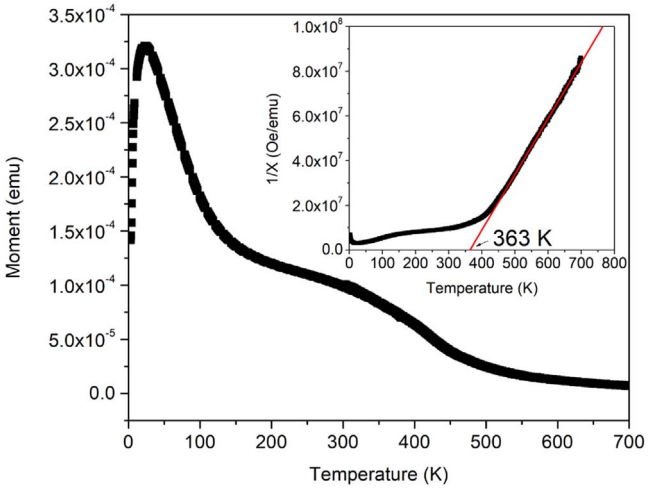

Figure 13. Temperature-dependent magnetization of PFOCr5 synthesized at 550 °C with Curie-Weiss graphical analysis (inset).

Cooling (ZFC) are shown. The ZFC curve reaches its peak value in the range of 22–40 K, with values between $2{\cdot}10^{-7}$ Am^2 and $4{\cdot}10^{-7}$ Am^2, independent of the chromium concentration. The bifurcation between the ZFC and FC curves occurs at a temperature slightly higher than room temperature (>310 K) for all samples. The coercivity at 5 K is related to the peak temperature of the ZFC susceptibility measurements of the films. The maximum value of the curves represents the average blocking temperature of superparamagnetic nanocrystals in the synthesized films. The wide temperature difference between the peak value and the bifurcation point in the ZFC-FC curves suggests a broad size distribution of the crystallites, where larger crystallites remain in the blocked state even at room temperature.

Figure 13 illustrates the temperature-dependent magnetization of PFOCr5 synthesized at 550 °C within the range of 300 to 700 K. This measurement was conducted using the specialized OVEN option of the QD PPMS. The determination of magnetic parameters is challenging due to the formation of small crystallites as mentioned earlier. Consequently, the Néel temperature in approximately 540 K range could not be identified. To determine the magnetic ordering temperature, Curie-Weiss graphical analysis was used for the high temperature range and transverse susceptibility straightening, as depicted in the inset of Fig. 13. The magnetic ordering temperature was found to be around 363 K. Based on the Néel temperature data, CrO_2 is a possible candidate for the magnetic ordering in chromium-doped PFO films.[39,40]

Conclusions

The study involved the synthesis of lead ferrite films doped with chromium using reactive magnetron sputtering in an oxygen environment. Structural, morphological, dielectric, and magnetic studies were carried out in different ranges of synthesis parameters. The lead ferrite phases were found in all samples at diffraction angle around 32°, and their intensity decreased with an increase in synthesis temperature due to lead desorption. Dielectric measurements showed that the highest polarization was recorded in PFOCr10 films, which reached 72.2 μC cm^{-2}. A positive correlation between Cr concentration and the increase of remanent polarization and coercive field was observed across all synthesis temperatures. Notably, the films synthesized at 600 °C exhibited the highest values of coercive field strength, with a maximum value of approximately 106 kV cm^{-1} observed in PFOCr10. The magnetization of PFOCr films was found to be up to $9.5{\cdot}10^{-7}$ Am^2 at an ambient temperature of 5 K. The orientation temperature of the magnetic properties of PFOCr was determined to be 363 K, which corresponds to the magnetic ordering temperature of chromium oxides. The morphology of PFOCr changed with increasing Cr content, with a decrease in grain size. Increasing the synthesis temperature also increased the size of the structures, forming denser films that correspond to the structural zone model.

Acknowledgments

The work at National Institute of Chemical Physics and Biophysics was supported by European Regional Development Fund project "Emerging orders in quantum and nanomaterials" (TK134) and the Estonian Research Agency (PRG1702).

ORCID

Benas Beklešovas https://orcid.org/0009-0008-4373-748X
Joosep Link https://orcid.org/0000-0001-6103-4034
Raivo Stern https://orcid.org/0000-0002-6724-9834

References

1. C. Gumiel and D. G. Calatayud, *Bol Soc Esp Ceram V*, **61**, 708 (2022).
2. I. H. Lone, J. Aslam, N. R. E. Radwan, A. H. Bashal, A. F. A. Ajlouni, and A. Akhter, *Nanoscale Res. Lett.*, **14**, 142 (2019).
3. D. I. Khomskii, *J. Magn. Magn. Mater.*, **306**, 1 (2006).
4. Y. Wang, J. Hu, Y. Lin, and C.-W. Nan, *NPG Asia Mater.*, **2**, 61 (2010).
5. S. R. Bae, D. Y. Heo, and S. Y. Kim, *Mater. Today Adv.*, **14**, 100232 (2022).
6. M. M. Vopson, *Crit. Rev. Solid State Mater. Sci.*, **40**, 223 (2015).
7. J. Wu, Z. Fan, D. Xiao, J. Zhu, and J. Wang, *Prog. Mater Sci.*, **84**, 335 (2016).
8. J. Shah, K. C. Verma, A. Agarwal, and R. K. Kotnala, *Mater. Chem. Phys.*, **239**, 122068 (2020).
9. S. Roy and S. B. Majumder, *J. Alloys Compd.*, **538**, 153 (2012).
10. M. S. Alkathy, A. Rahman, F. L. Zabotto, F. P. Milton, K. C. J. Raju, and J. A. Eiras, *Ceram. Int.*, **48**, 30041 (2022).
11. X. Ren, Y. Han, X. Chen, Y. Fu, F. Wang, K. Hu, Z. Sun, and K. Zhang, *J. Alloys Compd.*, **920**, 165918 (2022).
12. M. Wang and G. Tan, *Mater. Res. Bull.*, **46**, 438 (2011).
13. B. Beklešovas, V. Stankus, J. Link, and R. Stern, *Thin Solid Films*, **708**, 138124 (2020).
14. H. Deng, H. Deng, P. Yang, and J. Chu, *J. Mater. Sci., Mater. Electron.*, **23**, 1215 (2012).
15. B. Guo, H. Deng, X. Zhai, W. Zhou, X. Meng, G. Weng, S. Chen, P. Yang, and J. Chu, *Mater. Lett.*, **186**, 198 (2017).
16. S. K. Singh, K. Sato, K. Maruyama, and H. Ishiwara, *Jpn. J. Appl. Phys.*, **45**, L1087 (2006).
17. A. K. Sinha et al., *Results Phys.*, **13**, 102299 (2019).
18. F. Chang, N. Zhang, F. Yang, S. Wang, and G. Song, *J. Phys. D: Appl. Phys.*, **40**, 7799 (2007).
19. A. R. Makhdoom, M. J. Akhtar, M. A. Rafiq, M. Siddique, M. Iqbal, and M. M. Hasan, *AIP Adv.*, **4**, 037113 (2014).
20. S. Kumar et al., *Materials*, **15**, 4118 (2022).
21. M. Tefera Kebede, S. Devi, V. Dillu, and S. Chauhan, *Mater. Sci. Eng. B*, **283**, 115859 (2022).
22. A. M. Abakumov, J. Hadermann, S. Bals, I. V. Nikolaev, E. V. Antipov, and G. Van Tendeloo, *Angew. Chem. Int. Ed.*, **45**, 6697 (2006).
23. J. Hadermann, A. M. Abakumov, I. V. Nikolaev, E. V. Antipov, and G. Van Tendeloo, *Solid State Sci.*, **10**, 382 (2008).
24. I. V. Nikolaev et al., *Phys. Rev. B*, **78**, 024426 (2008).
25. M. M. Hoque, M. T. Islam, M. R. Islam, and M. A. Zubair, *Ceram. Int.*, **48**, 19583 (2022).

26. U. Khan, A. Nairan, M. Irfan, S. Naz, D. Wu, and J. Gao, *J. Alloys Compd.*, **912**, 165133 (2022).
27. A. Iljinas, L. Marcinauskas, and V. Stankus, *Appl. Surf. Sci.*, **381**, 6 (2016).
28. C. Millon, C. Malhaire, and D. Barbier, *Sens. Actuator A Phys.*, **113**, 376 (2004).
29. J. N. B. Sales et al., *Ceram. Int.*, **47**, 24564 (2021).
30. K. Sarkar, S. Mukherjee, and S. Mukherjee, *Process. Appl. Ceram.*, **9**, 53 (2015).
31. Y. Wang, W. Chen, B. Wang, and Y. Zheng, *Materials*, **7**, 6377 (2014).
32. A. Deepak Sharma and H. Basantakumar Sharma, *IOP Conf. Ser.: Mater. Sci. Eng.*, **1219**, 012052 (2022).
33. S. Sharma, S. Padmanapan, O. Pandey, and P. Sharma, *J. Mater. Sci., Mater. Electron.*, **27**, 5909 (2016).
34. V. R. Singh, A. Dixit, A. Garg, and D. Agrawal, *Appl. Phys. A*, **90**, 197 (2008).
35. S. M. Feng, Y. S. Chai, J. L. Zhu, N. Manivannan, Y. S. Oh, L. J. Wang, Y. S. Yang, C. Q. Jin, and K. H. Kim, *New J. Phys.*, **12**, 073006 (2010).
36. L. H. Yin et al., *Phys. Rev. B*, **98**, 054301 (2018).
37. X. Deng et al., *J. Mater. Sci., Mater. Electron.*, **30**, 16502 (2019).
38. A. Kumar, M. K. Warshi, A. Sagdeo, and P. R. Sagdeo, *J. Phys. Chem. C*, **125**, 14048 (2021).
39. Q. Chen and Z. J. Zhang, *Appl. Phys. Lett.*, **73**, 3156 (1998).
40. A. J. Rondinone, A. C. S. Samia, and Z. J. Zhang, *J. Phys. Chem. B*, **103**, 6876 (1999).